



Composition effects of spinel $Mn_xCo_{3-x}O_4$ nanoparticles on their electrocatalytic properties in oxygen reduction reaction in alkaline media

Eunjik Lee ^a, Ji-Hoon Jang ^a, Young-Uk Kwon ^{a, b, *}

^a SKKU Advanced Institute of Nanotechnology, Sungkyunkwan University, Suwon 440-746 Republic of Korea

^b Department of Chemistry, Sungkyunkwan University, Suwon 440-746 Republic of Korea



HIGHLIGHTS

- We synthesized $Mn_xCo_{3-x}O_4$ NP samples with $x = 0.0, 0.4, 0.8, 1.4, 1.9$, and 3.0 .
- The substituted Mn in sample is mainly on the Mn^{3+} ions in the octahedral site.
- The ORR mechanism is changed when the structure is changed from cubic to tetragonal.
- The highest ORR activity was observed with the $x = 0.4$ sample.
- The electrochemical stability of $x = 0.4$ sample is higher than that of Pt/C.

ARTICLE INFO

Article history:

Received 14 July 2014

Received in revised form

24 September 2014

Accepted 24 September 2014

Available online 2 October 2014

Keywords:

Metal oxide nanoparticles
Electrocatalyst
Alkaline fuel cells
Oxygen reduction reaction
Sonochemistry

ABSTRACT

In this work, we synthesized a series of manganese cobalt spinel oxide ($Mn_xCo_{3-x}O_4$) nanoparticles (NPs) covering the whole composition range ($x = 0.0, 0.4, 0.8, 1.4, 1.9$, and 3.0) and investigated their electrocatalytic properties in relation with the oxygen reduction reaction (ORR) in alkaline media. The NP samples were synthesized by sonochemical reactions of $Mn(OAc)_2$ and $Co(OAc)_2$ (Ac = acetyl) in a water-dimethylformamide mixed solvent. The four samples in the Co-rich side have the cubic structure whereas the other two samples in the Mn-rich side have the tetragonal structure. The X-ray photoelectron spectroscopy and electrochemical analyses data indicate that the distribution of manganese and cobalt ions between the two metal ion sites of the spinel structure in our NP samples conforms to that of the bulk counterparts in the literature. The electrocatalytic data show that the ORR mechanism is changed when the structure is changed from cubic to tetragonal. The highest ORR activity was observed with the $x = 0.4$ sample. The electrochemical stability of this sample is higher than that of commercial Pt/C.

© 2014 Elsevier B.V. All rights reserved.

1. Introduction

Oxygen reduction reaction (ORR) is a key process in energy conversion and storage systems such as fuel cells and metal-air batteries [1–5]. The development of highly efficient electrocatalysts to be used at the cathode has been an important issue because of the sluggish kinetics and the high overpotential of ORR. Typically, Pt nanoparticles (NPs) supported on porous carbon have

been considered as electrocatalyst for their relatively low overpotentials for ORR. However, the high cost and limited resources of Pt are major challenges for commercialization.

Recently, electrocatalysts based on non-precious materials have been investigated to replace Pt. In many literature works, various nitrogen-doped carbon materials, oxide materials especially with the spinel-type and perovskite-type structures, and macrocyclic complexes have been synthesized and tested as candidates for ORR electrocatalysts [6–9]. Among these, transition metal spinel oxides such as Co_3O_4 and Mn_3O_4 exhibit promising ORR activity in alkaline media, comparable to that of Pt [5,10]. In addition, ORR activity of various mixed metal spinel oxides (i.e., $MnCo_2O_4$, $NiCo_2O_4$, and $MnFe_2O_4$) has been investigated [11–13]. According to these

* Corresponding author. SKKU Advanced Institute of Nanotechnology, Department of Chemistry, Sungkyunkwan University, Suwon 440-746 Republic of Korea. Tel.: +82 31 290 7070; fax: +82 31 290 7075.

E-mail address: ywkwon@skku.edu (Y.-U. Kwon).

reports, the mixed metal oxides showed enhanced electrochemical properties from single metal oxides for ORR. Generally, mixed metal oxides have good electrical conductivities through electron hopping, which can contribute to the enhancement of electrocatalytic activity [13,14].

The present work is on $Mn_xCo_{3-x}O_4$ spinel oxide NPs and the effect of composition on the ORR activity in alkaline media. Spinel oxides have the general formula $(A)[B]_2O_4$. The structure is often described as a cubic close-packed arrangement of O^{2-} ions with the A and B sites, respectively, representing one eighth of the tetrahedral and a half of the octahedral interstitial sites. The A and B sites are typically occupied by one divalent and two trivalent ions. Their distribution between the tetrahedral and octahedral sites depends on the electronic structures of the ions and other factors, which can be a means to control the properties of spinel oxides [15,16].

Because of the aforementioned beneficial effects of mixed metal oxides, electrocatalysis on $Mn_xCo_{3-x}O_4$ has attracted some interests. For instance, Gautier et al. reported that ORR activity of $Mn_xCo_{3-x}O_4$ ($x = 0.0\text{--}1.0$) thin films increases as the Mn content increases [17]. Various synthetic techniques have been used to synthesize $Mn_xCo_{3-x}O_4$ NPs including sol–gel process, solvothermal method, and thermal decomposition of CoMn layered double hydroxide [18–20]. However, the electrocatalytic properties have been investigated only on a few selected compositions probably because each one of these methods has limitations in covering the whole composition range. Although the solid solution in the whole composition range has been synthesized by the ceramic method, the samples generally have very small surface areas, unsuitable for electrocatalysis studies [21].

Here, we synthesized $Mn_xCo_{3-x}O_4$ NP samples covering the whole range of composition ($x = 0.0, 0.4, 0.8, 1.4, 1.9$, and 3.0) using a sonochemical reaction method. Structural and electrochemical analyses of the samples were performed to understand the effects of composition to their ORR activity.

2. Experimental

2.1. Preparation of $Mn_xCo_{3-x}O_4$ NP samples

Mn-substituted cobalt oxides with various compositions were synthesized by sonochemical reactions. First, $Co(OAc)_2$ (Fluka), $Mn(OAc)_2$ (Fluka), and 0.02 g of porous carbon (Ketjen Black 300 J) were added into a mixed solvent of dimethylformamide (30 mL) and distilled water (5 mL). The amounts of metal precursors were adjusted from 0 to 1.5 mmol for both $Co(OAc)_2$ and $Mn(OAc)_2$. The dispersion solution was irradiated by a high-intensity ultrasound (Sonic and Materials, VC-500; 30% amplitude; 20 kHz ; 13 mm solid probe) for 2 h . The reaction temperature was kept at $130\text{ }^\circ\text{C}$ by an external heating. After the sonochemical reaction, the product slurry was filtered, washed with excess ethanol and dried under a vacuum.

2.2. Electrochemical measurements

5 mg of a sample was put into 2.5 mL of distilled water and then the solution was sonicated until a homogeneous suspension was formed. $5\text{ }\mu\text{L}$ of the suspension was loaded on a glassy carbon electrode ($d = 3\text{ mm}$, area = 0.0707 cm^2) to form a thin film and dried at room temperature. To prevent the loss of sample into electrolyte, $5\text{ }\mu\text{L}$ of a 0.05 wt. \% Nafion solution was dropped over the thin film on glassy carbon electrode.

Electrochemical analyses were conducted by a potentiostat (Ivium compactstat, Ivium technology) with a standard three electrode electrochemical cell. A $Ag/AgCl$ (sat'd KCl) and a Pt net

were used for reference and counter electrodes, respectively. Before each electrochemical measurement, the working electrode was cleaned by potential cycling for 50 cycles between -0.6 V and 0.0 V (vs. $Ag/AgCl$). Cyclic voltammograms (CVs) were recorded in a N_2 saturated 0.1 M KOH aqueous solution at a scan rate of 50 mV s^{-1} . Linear sweep voltammograms (LSVs) were recorded in a O_2 saturated 0.1 M KOH aqueous solution at a scan rate of 10 mV s^{-1} . Chronoamperometry was measured to evaluate the electrochemical durability of electrocatalysts at -0.5 V (vs. $Ag/AgCl$) for $10,000\text{ s}$. The potential ranges in the present work are referred to the reversible hydrogen electrode (RHE).

2.3. Characterization

Powder X-ray diffraction (XRD) measurements were performed using an Ultima IV X-ray diffractometer (Rigaku, $CuK\alpha$, $\lambda = 1.54056\text{ \AA}$). The microstructures and elemental distribution of samples were observed by transmission electron microscopy (TEM, JEOL JEM-3011 model, 300 kV) and scanning transmission electron microscopy (STEM, JEOL JEM-ARM200F, 200 kV). X-ray photoelectron spectroscopy (XPS, VG Microtech EDCA2000) measurements were performed with a monochromatic $Mg K\alpha$ source (1253.6 eV). The elemental compositions were determined by energy dispersive X-ray spectroscopy (EDS) using an EDS analyzer attached on a scanning electron microscope (SEM, JEOL JSM-7100). Five different spots were measured to obtain averaged composition for each sample.

3. Results and discussion

We synthesized a series of $Mn_xCo_{3-x}O_4$ NP samples covering the whole range of the solid solution $Co_3O_4\text{--}Mn_3O_4$. There have been similar studies in terms of the coverage of the composition range, but all of them are by high temperature solid state reactions, precluding their characterization as electrocatalyst materials [21–23]. Some members of the solid solution have been synthesized in NP forms and investigated as electrocatalysts, but their compositional coverage is fragmentary [17,24].

Based on the EDS data, the samples have compositions $Mn_xCo_{3-x}O_4$ ($x = 0.0, 0.4, 0.8, 1.4, 1.9$, and 3.0) (Table 1). The formation of spinel oxide NPs can be understood as a result of a series

Table 1
The structural and electrochemical characteristic of electrocatalyst.

Sample	Crystallite size (nm) ^a	Lattice parameter(nm) ^b	Elemental composition (at. %) ^c		Electrochemical performance	
			Mn:Co	σ	Current density ^d (mA cm^{-2})	Current retention ^e (%) ^c
$x = 0.0$	17.2	$a = 0.815$	0:100	—	-1.10	80.3
$x = 0.4$	17.0	$a = 0.820$	13.4:86.6	0.2	-2.77	87.1
$x = 0.8$	14.7	$a = 0.825$	25.4:74.6	0.2	-2.32	75.9
$x = 1.4$	11.0	$a = 0.828$	46.4:53.6	0.4	-1.89	72.5
$x = 1.9$	7.2	$a = 0.578,$ $c = 0.912$	62.5:37.5	0.6	-2.09	65.5
$x = 3.0$	11.8	$a = 0.577,$ $c = 0.949$	100:0	—	-0.22	75
Pt/C	—	—	—	—	-4.15	62.6

^a Crystallite size of samples are calculated by Scherrer formula.

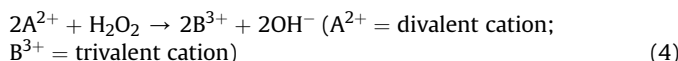
^b Lattice parameter of samples are determined from XRD.

^c Elemental composition of samples were determined by averaging of five different spots of EDS data.

^d Current density of samples at 0.77 V in LSVs plot.

^e Current retention of samples were obtained by current normalization before and after stability test for $10,000\text{ s}$.

of reactions initiated by rupturing the chemical bonds of H_2O molecules under the action of ultrasound to generate $\text{H}\cdot$ and $\text{OH}\cdot$ radicals [25,26]. Two $\text{OH}\cdot$ radicals so formed are combined to form a H_2O_2 molecule which can oxidize a divalent cation (M^{2+}) into a trivalent cation (M^{3+}). The metal ions so generated undergo reactions with water molecules to form oxide or hydroxide compounds [27]. The overall reactions may be expressed as in the following equations:



Depending on the nature of the metal ions and other reaction parameters including pH, especially, the final product may change. In the present system, both Mn and Co can generate divalent and trivalent cations and the pH can be kept high by the OH^- ions generated by reaction (4), under which condition spinel oxide would be the most favorable product.

The XRD patterns of samples in Fig. 1 show two types of spinel phases depending on the composition. When the Mn-content is low ($0.0 \leq x \leq 1.4$), the XRD patterns can be indexed with cubic unit cells whereas tetragonal phases are obtained when the Mn-content is high ($x = 1.9$ and 3.0). Among the four cubic samples, the lattice parameter is gradually increased from $a = 0.815$ ($x = 0.0$) to $a = 0.825$ nm ($x = 1.4$) as the Mn-content increases, which can be explained by the larger ionic sizes of Mn than Co in both divalent and trivalent states. This trend of increasing unit cell volume is continued in the tetragonal phases. By using the Scherrer equation on the widths of the peaks at $2\theta = \sim 36^\circ$, (220) peak in the cubic phase and (211) peak in the tetragonal phase, the average crystallite sizes are calculated as shown in Table 1. The crystallite sizes show a general trend of decrease on increasing the Mn-content with an upturn between the last two members, $x = 1.9$ and $x = 3.0$ samples.

Fig. 2 shows TEM images of $\text{Mn}_x\text{Co}_{3-x}\text{O}_4$ samples. The low magnification image of $x = 0.0$ sample (Co_3O_4) shows that

50–60 nm sized particles are dispersed on the carbon support. However, the high magnification image in Fig. S1 shows that these particles are, in fact, aggregates of much smaller NPs. On the contrary, all of the Mn-containing ($x = 0.4$ – 3.0) samples show that individual NPs are well-dispersed on the carbon support (Fig. 2(b–f)).

The reason for the aggregation of NPs observed in the $x = 0.0$ sample is not clear. However, since such aggregation is not observed in other Mn-containing samples, it is obvious that the presence of Mn prevents the formation of aggregation. Furthermore, it is certain that the aggregation is through interaction between Co atoms of interacting NPs and that Mn atoms do not have such a property. Therefore, the presence of Mn increases the degree of dispersion of NPs.

STEM-EDS elemental mapping of $x = 0.4$ sample was measured to confirm the elemental composition and homogeneity of manganese and cobalt distribution. Fig. 3(c,d) show that manganese and cobalt are homogenously mixed throughout the sample.

The XPS spectra of Co 2p and Mn 2p regions on the four cubic phase samples ($x = 0.0$ – 1.4) are shown in Fig. 4. The Co 2p spectra can be de-convoluted into those of Co^{3+} and Co^{2+} (Fig. 4(a)). As the Mn content increases, the intensity of Co^{3+} is gradually decreased. At the same time, the intensity of $\text{Mn} 2\text{p}_{3/2}$ at 641.8 eV is increased (Fig. 4(b)). Unlike the Co 2p spectra, the positions of the $\text{Mn} 2\text{p}_{1/2}$ and $\text{Mn} 2\text{p}_{3/2}$ peaks of Mn^{2+} and Mn^{3+} are so close to each other that de-convoluting the peaks into the Mn^{2+} and Mn^{3+} components is almost impossible (Fig. 4(b)). Fortunately, most of the literature data on $\text{Mn}_x\text{Co}_{3-x}\text{O}_4$ solid solution in both bulk state and NPs show that Mn is present as Mn^{3+} up to $x = 2.0$ [23,28]. Therefore, we can conclude that the substitution of Co in Co_3O_4 by Mn takes place exclusively on the trivalent ions.

From detailed analyses of neutron diffraction data on bulk phase samples of $\text{Mn}_x\text{Co}_{3-x}\text{O}_4$, Bordeneuve et al. determined the site occupancies and oxidation states of Co and Mn ions, which are schematically summarized in Figure S2 [23]. Until $x = 2.0$, the substitution of Co by Mn takes place on the octahedral site to form $(\text{Co}^{2+})[\text{Co}^{3+}_{2-x}\text{Mn}^{3+}_x]\text{O}_4$. A fraction of the Co^{3+} – Mn^{3+} pairs in the octahedral sites undergo internal redox reactions to produce Co^{2+} – Mn^{4+} pairs. The extent of this reaction (α in Figure S2) can be as high as 0.4 when $x = \sim 0.9$. At $x = 2.0$, $(\text{Co}^{2+})[\text{Mn}^{3+}_2]\text{O}_4$ is obtained. Beyond this, Co^{2+} ions in the tetrahedral site start to be replaced by Mn^{2+} until $(\text{Mn}^{2+})[\text{Mn}^{3+}_2]\text{O}_4$ composition is reached for $x = 3.0$ sample. The increase of concentration of Mn^{3+} induces Jahn–Teller distortion from the ideal octahedral geometry of CoO_6 . Therefore, the structure is cubic when the Mn-content is low ($x \leq \sim 1.3$) and is tetragonal when the Mn-content is high ($x \geq \sim 1.3$). Our XRD and XPS data generally agree with their results. Although the $x = 1.4$ sample is indexed as cubic, its true structure may be tetragonal as in the bulk system. However, because of the broad peaks due to the nanoparticle nature of our sample, it is impossible to decide its true structure. We will treat it as cubic because there is no experimental evidence indicating otherwise.

It is known that, in the electrocatalysis of spinel oxides for ORR, the ions in the octahedral sites play an important role through the involvement of their d-orbitals in the chemisorptions of O_2 on the surface [17,29]. Therefore, the change of composition of the present $\text{Mn}_x\text{Co}_{3-x}\text{O}_4$ NPs will be reflected in their ORR activity.

Electrochemical properties of samples were measured to evaluate ORR activity in 0.1 M KOH by using rotating disk electrode (RDE) measurements. The CV curve of $x = 0.0$ sample in N_2 saturated 0.1 M KOH shows the characteristic three sets of redox peaks of cobalt oxide (Fig. 5(a)). The peaks are assigned to the following reactions [11].

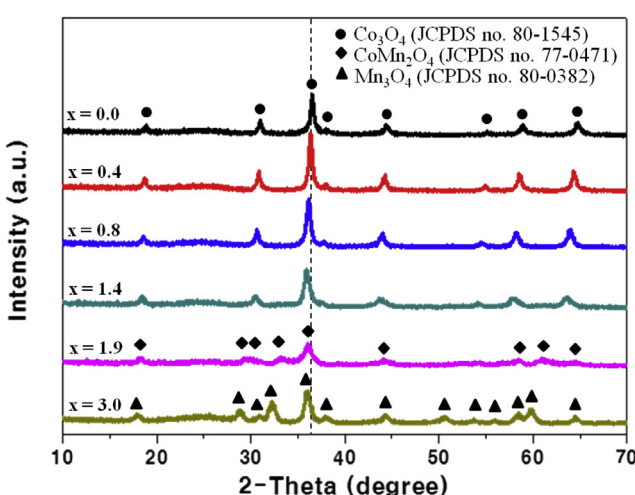


Fig. 1. XRD patterns of $\text{Mn}_x\text{Co}_{3-x}\text{O}_4$ samples. Dash line indicates the (311) peak of Co_3O_4 .

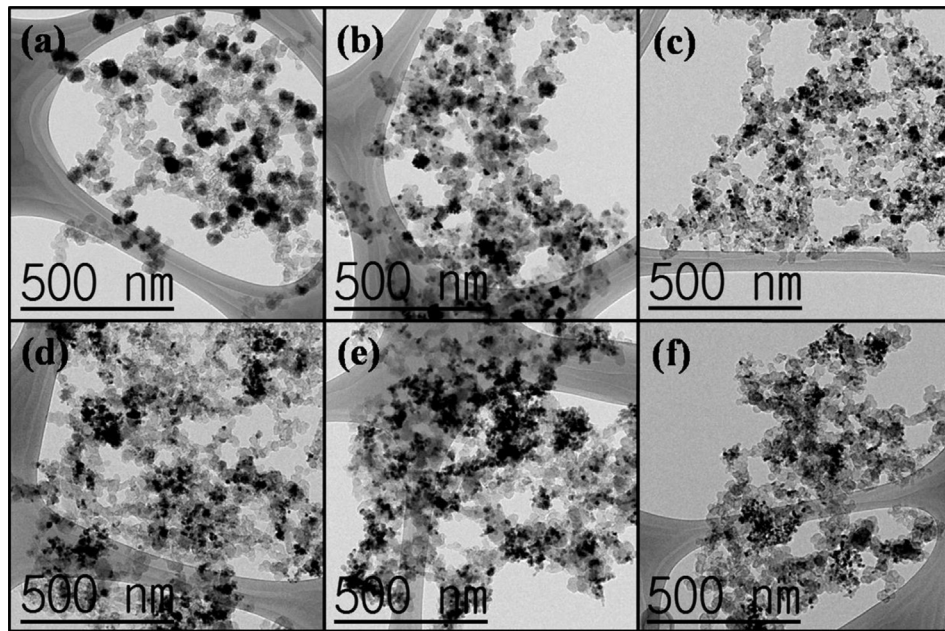


Fig. 2. TEM images of $\text{Mn}_x\text{Co}_{3-x}\text{O}_4$ samples (a) $x = 0.0$, (b) $x = 0.4$, (c) $x = 0.8$, (d) $x = 1.4$, (e) $x = 1.9$ and (f) $x = 3.0$.

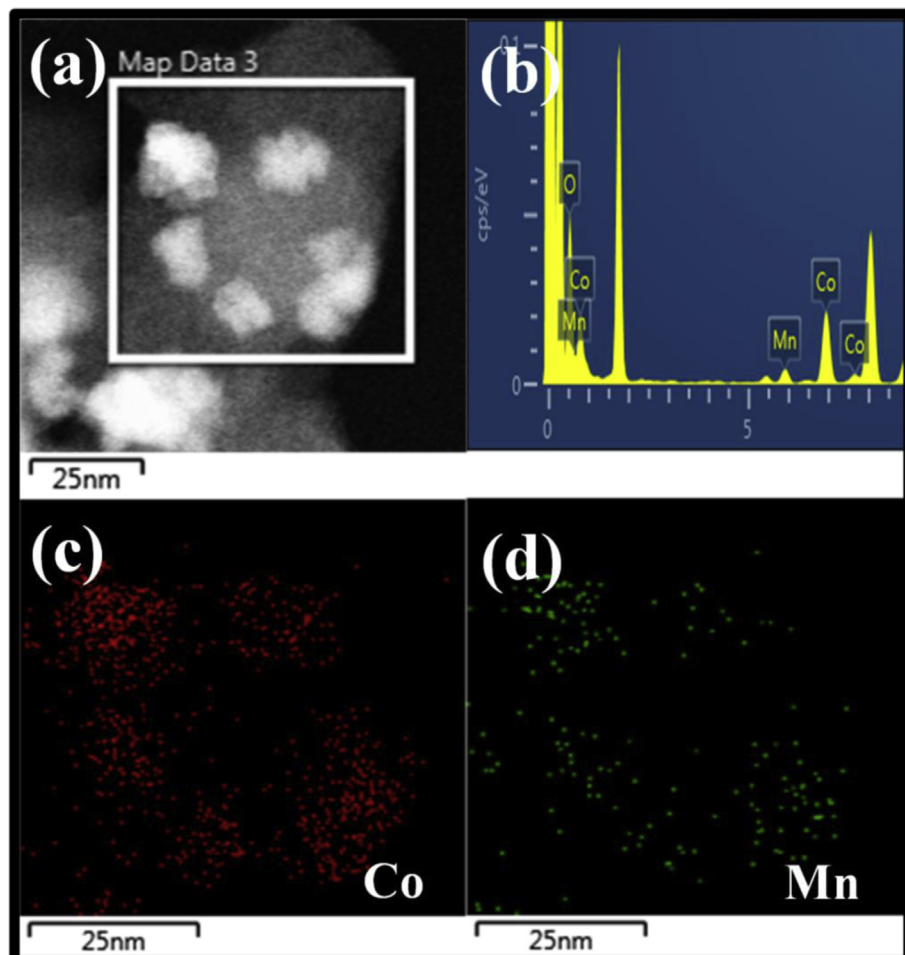


Fig. 3. STEM-EDS elemental mapping of $x = 0.4$ sample. (a) Image of selected area, (b) EDS spectrum, (c) Co K α map and (d) Mn K α map.

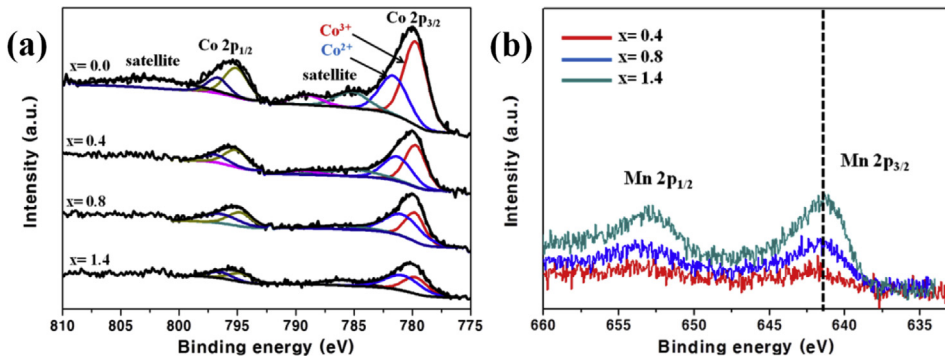
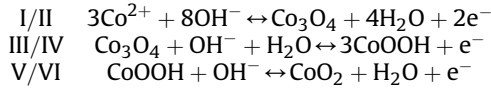


Fig. 4. XPS spectra of cubic phase $\text{Mn}_x\text{Co}_{3-x}\text{O}_4$ samples. (a) Co 2p regions and (b) Mn 2p regions. Dashed line indicates the peak position of Mn^{3+} .



Compared with the first two sets of redox peaks, the oxidation of CoOOH (peak V) is much more pronounced in the potential range from 0.9 V to 1.6 V. The reason is that the Co_3O_4 surface layer is spontaneously converted to CoOOH in alkaline media [11]. Fig. 5(b) shows the CV curves of other Mn-containing samples ($x = 0.4\text{--}3.0$). Interestingly, the oxidation peak of Co_3O_4 at 1.22 V (peak III in Fig. 5(a)) disappears with the addition of Mn whereas the oxidation peak of Co^{2+} (peak I) still exists at around 0.97 V. This indicates that the substitution of Mn occurs on the trivalent site. This observation is consistent with our XPS results and literature data in that the substitution of Mn occurs on the trivalent site. The CV curves of Mn-rich samples from $x = 1.4$ to $x = 3.0$ at the potential range from 0.8 V to 1.4 V also show the large oxidation peak compared with the Co-rich samples ($x = 0.4$ and 0.8). This broad peak can be assigned to the oxidation of MnOOH to MnO_2 [30] due to the increased proportion of Mn^{3+} on the NP surface. This peak shows a positive shift on moving from $x = 1.4$ to $x = 3.0$. We believe that the peak shift is related with the degree of Jahn–Teller distortion of the octahedral site. Mn^{3+} (d⁴, high spin) ions in the present $\text{Mn}_x\text{Co}_{3-x}\text{O}_4$ can be stabilized by Jahn–Teller distortion. Therefore, as the degree of Jahn–Teller distortion is increased upon increasing x in the tetragonal structure, oxidation of Mn^{3+} to Mn^{4+} becomes more difficult, explaining the observed trend in Fig. 5(b) [31].

The ORR properties of samples were investigated by LSVs in O_2 -saturated 0.1 M KOH, and are compared in Fig. 5(c) along with that of a commercial Pt C⁻¹. Each LSV curve shows the diffusion-limited region at potentials below ~0.55 V and the mixed kinetic-diffusion control region at 0.55–0.95 V. The curves of the cubic phase ($x = 0.0\text{--}1.4$) samples are more or less similar with one another and thus are grouped in the upper panel of this figure. All of them show high diffusion-limited current densities (DLCDs) of ~5 mA cm⁻² and similar slopes in the mixed kinetic-diffusion control region. The two tetragonal samples show very different LSV curves (lower panel in Fig. 5(c)) from those of the cubic samples. They have smaller DLCDs of ~4 mA cm⁻². Their behaviors in the mixed kinetic-diffusion control region are also different from those of the cubic samples and are also very different between them. The DLCD depends on electron transfer number (ORR pathway) as well as rotating speed of RDE [20]. Therefore, the higher ORR current density of the cubic samples indicates that they have a more efficient ORR pathway than the tetragonal samples. To verify the different ORR pathways, Koutecky–Levich plots of samples were obtained from LSV curves with various rotating speeds (Figure S3). Figure S4(a) shows that the cubic samples have a higher electron transfer number (~4) than the tetragonal ones (~3.5). In addition,

the slopes of the cubic samples are parallel to that of Pt/C at 0.37 V (Figure S4(b)).

Conventionally, the half-wave potential ($E_{1/2}$) is used in comparing different samples for ORR activity. In the present case, however, because of the different DLCDs between the two groups of samples, $E_{1/2}$ may not be a reliable measure to compare across the groups. Therefore, $E_{1/2}$ will be used for comparison within a group. Among the four cubic samples, the order of $E_{1/2}$ is $x = 0.4$ (0.772 V) > 0.8 (0.764 V) > 1.4 (0.753 V) > 0.0 (0.715 V). Incorporation of a small amount of Mn ($x \sim 0.4$) increases $E_{1/2}$, but further increase of Mn-content decreases $E_{1/2}$. Between the two tetragonal samples, the one with Co mixed shows a much higher $E_{1/2}$ than pure Mn_3O_4 ($x = 3.0$).

Generally, detailed mechanism of electrocatalysis on oxide materials have not been well explored yet. Therefore, explanation of the electrocatalytic data on $\text{Mn}_x\text{Co}_{3-x}\text{O}_4$ NPs is bound to be limited and often speculative. Nevertheless, we will give our explanations on the observed data on the ground of the mechanism proposed by Suntivich et al. [8]. From a systematic study on perovskite type oxides, they found that transition metal ions with a single electron in the e_g level in the octahedrally splitted d-orbitals (or e -level when the surrounding symmetry is lower than octahedral) are particularly active. The e -electron induces weakening of $\text{M}-\text{OH}$ bond and is also involved in coordinating to and reducing O_2 , enabling a series of reactions in a catalytic cycle to work. The single e -electron (e^1) configuration can be realized with high spin Mn^{3+} (t^3e^1) and low spin Co^{3+} on surface (t^5e^1 ; surface ionic state is different from the bulk configuration t^6e^0). According to this mechanism, both of the Co^{3+} and Mn^{3+} ions in our $\text{Mn}_x\text{Co}_{3-x}\text{O}_4$ system can be catalytically active.

The striking different ORR properties of the two tetragonal samples can be readily explained by this mechanism. According to the site occupancy in $\text{Mn}_x\text{Co}_{3-x}\text{O}_4$ in Figure S2, both $x = 1.9$ and 3.0 samples have only Mn^{3+} ions in the octahedral site. Because $x = 3.0$ sample show a larger tetragonal distortion, one can infer a stronger Jahn–Teller distortion of the coordination environment of Mn^{3+} in this sample than in the $x = 1.9$ sample. Jahn–Teller distortion on a high spin Mn^{3+} means stabilization of the e^1 electron. Based on the catalytic cycle proposed by Suntivich et al., this will strongly disfavor the reductive coordination to O_2 suppressing the ORR activity. Conversely, the higher activity of $x = 1.9$ sample than $x = 3.0$ sample can be explained as due to the small degree of Jahn–Teller distortion, destabilizing the e^1 electron by an appropriate magnitude.

The trend of ORR activity among the four cubic samples appears to be much more involved. According to the site occupancy in Figure S2, the change of x means substituting catalytically active Co^{3+} by catalytically active Mn^{3+} . Unless one can tell which one is more active than the other, it is impossible to predict the

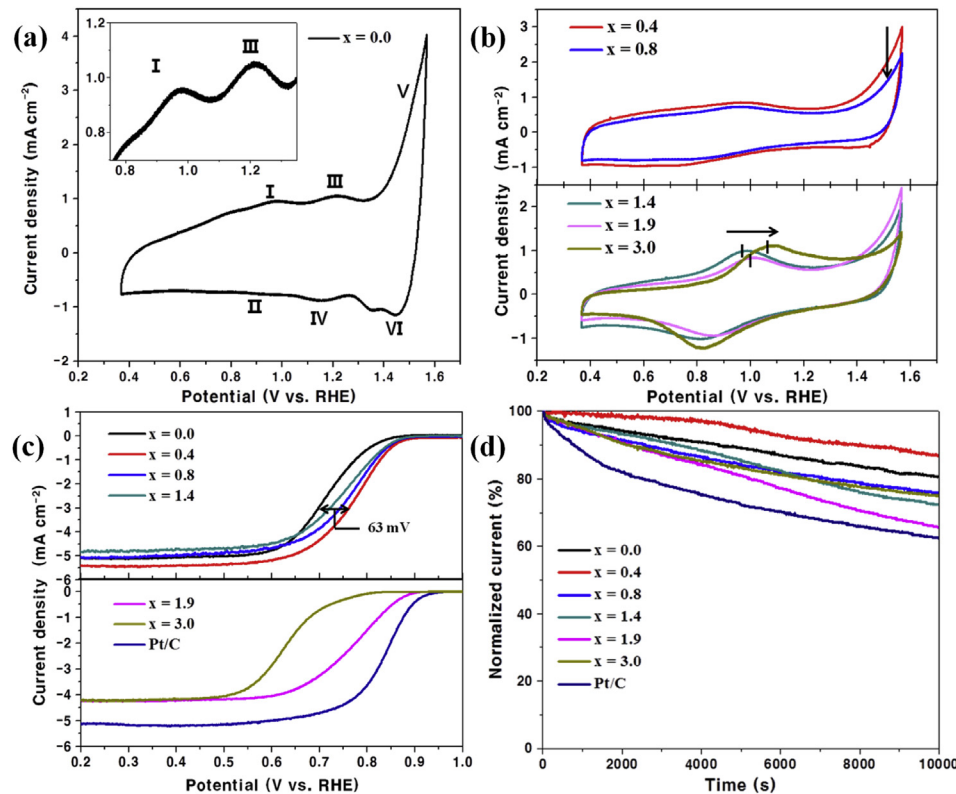


Fig. 5. CVs plots of (a) $x = 0.0$ sample and (b) other samples in N_2 -saturated 0.1 M KOH (scan rate; 50 mV s^{-1}). Each inset shows the magnified CVs curves. (c) LSVs plots of samples in O_2 -saturated 0.1 M KOH (scan rate: 10 mV s^{-1} , 1600 rpm). (d) Chronoamperometric curves of samples were recorded at 0.47 V in O_2 -saturated 0.1 M KOH (1600 rpm, 10,000 s).

consequences of the substitution. On the other hand, one may include other effects such as conductivity and surface area. The bulk state data show that the conductivity increases on increasing x and then decreases after peaking at $x = \sim 1.2$. Based on the decreasing trend of crystallite size with the increase of x , one may infer that the surface area continuously increases with x within the cubic region. With these two factors alone, one may expect the ORR activity to increase with x within the group of cubic samples or the ORR highest activity with the $x = 1.4$ sample which is the highest in conductivity. Certainly, there must be an additional factor that influences the activity to see that the highest catalytic activity is observed with $x = 0.4$ sample. Our tentative explanation involves the change of the crystal field splitting energy with the composition in Figure S2. In order to activate the catalytic cycle involved in ORR, each elementary interaction has to be optimized, not maximized. As the lattice expands with the increase of Mn-content, the crystal field splitting energy will decrease. Because e-level is of anti-bonding character, the e-level energy will be lowered with the increase of x . Assuming that the appropriate energy level of the e¹ electron for the catalytic cycle is high, the activity per site will decrease with the increase of x . The interplay between this and the two factors discussed above can bring in the observed volcano-type overall behavior of ORR.

To evaluate the stability of samples, chronoamperometric currents of samples were recorded at 0.47 V for 10,000 s as shown in Fig. 5(d). The current retention before and after the stability test of each sample is summarized in Table 1. All samples show higher electrochemical stability than Pt/C. In case of Pt/C, surface oxidation occurs spontaneously in alkaline media and the Pt–OH species so formed on the surface leads to the loss of active sites for ORR [11,13,32]. The higher stability of $Mn_xCo_{3-x}O_4$ NPs indicates that there is no such reaction on them.

4. Conclusion

In summary, we synthesized manganese cobalt spinel oxide ($Mn_xCo_{3-x}O_4$) NPs and investigated their ORR activity in alkaline media. Sonochemical reaction method provides a means to synthesize samples covering the entire composition range and enables one to see the effect of composition. From the structural and electrochemical analyses, we found that the substitution of Co in Co_3O_4 by Mn in our NP samples occur in the similar way as in the bulk samples in the literature. There are a number of factors that change with the composition. From the study on bulk samples, it is concluded that the Co^{3+} and Mn^{3+} ions in the octahedral site when $x \leq 2.0$ undergo internal redox reaction to produce Co^{2+} and Mn^{4+} pairs, which increase the conductivity. The electronic states of catalytically active ions are also affected by the composition mainly because Mn is larger than Co and that Mn^{3+} favors Jahn–Teller distortion. Our data show that the $x = 0.4$ cubic sample has the highest ORR activity among the samples studied. It also shows enhanced stability over that of Pt.

Acknowledgments

This work was supported by grants NRF-20090081018 (Basic Science Research Program), NRF-2009-0094023 (Priority Research Center Program), and NRF-2009-0083540 (Basic Science Research Program). We thank CCRF for the TEM.

Appendix A. Supplementary data

Supplementary data related to this article can be found at <http://dx.doi.org/10.1016/j.jpowsour.2014.09.156>.

References

- [1] B. Wang, J. Power Sources 152 (2005) 1.
- [2] Q. Tang, L. Jiang, J. Liu, S. Wang, G. Sun, ACS Catal. 4 (2014) 457.
- [3] Z. Yang, H. Nie, X. Chen, X. Chen, S. Huang, J. Power Sources 236 (2013) 238.
- [4] J.-H. Jang, E. Lee, J. Park, G. Kim, S. Hong, Y.-U. Kwon, Sci. Rep. 3 (2013) 2872.
- [5] M. Hamdani, R.N. Singh, P. Chartier, Int. J. Electrochem. Sci. 5 (2010) 556.
- [6] N.P. Subramanian, X. Li, V. Nallathambi, S.P. Kumaraguru, H. Colon-Mercado, G. Wu, J.-W. Lee, B.N. Popov, J. Power Sources 188 (2009) 38.
- [7] Y. Wang, X. Cui, L. Chen, C. Wei, F. Cui, H. Yao, J. Shi, Y. Li, Dalton Trans. 43 (2014) 4163.
- [8] J. Suntivich, H.A. Gasteiger, N. Yabuuchi, H. Nakanishi, J.B. Goodenough, Y. Shao-Horn, Nat. Chem. 3 (2011) 546.
- [9] R. Liu, C. von Malotki, L. Arnold, N. Koschno, H. Higashimura, M. Baumgarten, K. Müllen, J. Am. Chem. Soc. 133 (2011) 10372.
- [10] Y.-G. Wang, L. Cheng, F. Li, H.-M., Xiong, Y.-Y. Xia, Chem. Mater. 19 (2007) 2095.
- [11] Y. Liang, H. Wang, P. Diao, W. Chang, G. Hong, Y. Li, M. Gong, L. Xie, J. Zhou, J. Wang, T.Z. Regier, F. Wei, H. Dai, J. Am. Chem. Soc. 134 (2012) 15849.
- [12] C. Jin, F. Lu, X. Cao, Z. Yang, R. Yang, J. Mater. Chem. A 1 (2013) 12170.
- [13] H. Zhu, S. Zhang, Y.-X. Huang, L. Wu, S. Sun, Nano Lett. 13 (2013) 2947.
- [14] C.-C. Kuo, W.-J. Lan, C.-H. Chen, Nanoscale 6 (2014) 334.
- [15] M.-C. Yang, B. Xu, J.-H. Cheng, C.-J. Pan, B.-J. Hwang, Y.S. Meng, Chem. Mater. 23 (2011) 2832.
- [16] P.F. Ndione, Y. Shi, V. Stevanovic, S. Lany, A. Zakutayev, P.A. Parilla, J.D. Perkins, J.J. Berry, D.S. Ginley, M.F. Toney, Adv. Funct. Mater. 24 (2014) 610.
- [17] A. Restovic, E. Rios, S. Barbato, J. Ortiz, J.L. Gautier, J. Electroanal. Chem. 522 (2002) 141.
- [18] P. Lavela, J.L. Tirado, C. Vidal-Abarca, Electrochim. Acta 52 (2007) 7986.
- [19] Y. Matsushita, H. Ueda, Y. Ueda, Nat. Mater. 4 (2005) 845.
- [20] D. Wang, X. Chen, D.G. Evans, W. Yang, Nanoscale 5 (2013) 5312.
- [21] J.M.J. Mateos, J. Morales, J.L. Tirado, J. Solid State Chem. 82 (1989) 87.
- [22] H. Bordeneuve, S. Guillemet-Fritsch, A. Rousset, S. Schuurman, V. Poulaire, J. Solid State Chem. 182 (2009) 396.
- [23] H. Bordeneuve, C. Tenailleau, S. Guillemet-Fritsch, R. Smith, E. Suard, A. Rousset, Solid State Sci. 12 (2010) 379.
- [24] M. Sugawara, M. Ohno, K. Matsuki, J. Mater. Chem. 7 (1997) 833.
- [25] R.V. Kumar, Y. Diamant, A. Gedanken, Chem. Mater. 12 (2000) 2301.
- [26] J.H. Bang, K.S. Suslick, Adv. Mater. 22 (2010) 1039.
- [27] P. Cousin, R.A. Ross, Mater. Sci. Eng. A 130 (1990) 119.
- [28] Y. Liang, H. Wang, J. Zhou, Y. Li, J. Wang, T. Regier, H. Dai, J. Am. Chem. Soc. 134 (2012) 3517.
- [29] J. Xu, P. Gao, T.S. Zhao, Energy Environ. Sci. 5 (2012) 5333.
- [30] K. Subramani, D. Jeyakumar, M. Sathish, Phy. Chem. Chem. Phys. 16 (2014) 4952.
- [31] D.P. Shoemaker, J. Li, R. Seshadri, J. Am. Chem. Soc. 131 (2009) 11450.
- [32] Y. Liang, Y. Li, H. Wang, J. Zhou, J. Wang, T. Regier, H. Dai, Nat. Mater. 10 (2011) 780.